

Supporting Information

A Predictive Mathematical Framework for Hemoglobin-Material Interactions: Development of the Hemoglobin Sensitivity Index (HSI) for Next-Generation Biomedical Applications

Navid Rabiee^{1,*}, Mohammad Edrisi²

1. Department of Biomaterials, Saveetha Dental College and Hospitals, SIMATS, Saveetha University, Chennai, 600077, India
2. Institute of Biochemistry and Biophysics (IBB), University of Tehran, Tehran, Iran

*Corresponding author: Dr. Navid Rabiee (nrabiee94@gmail.com)

S1. Computational Infrastructure, Methodology Framework and Model Construction

The HSI framework implementation relies on a comprehensive computational infrastructure designed to handle the complex multi-scale modeling requirements spanning quantum mechanical calculations, molecular dynamics simulations, statistical mechanical analyses, and machine learning optimization procedures. The computational architecture was constructed using a hybrid high-performance computing approach that integrates specialized software packages, custom-developed algorithms, and distributed computing resources to ensure both computational accuracy and scalability across diverse material classes and application contexts. All quantum mechanical calculations were performed using Gaussian 16 (Revision C.01) and ORCA 5.0.3 software packages, with density functional theory computations utilizing the B3LYP hybrid functional combined with the 6-311G** basis set for main group elements and the LANL2DZ effective core potential for transition metals, ensuring consistent treatment of electronic structure across organic and inorganic materials. Molecular dynamics simulations were conducted using GROMACS 2022.3 and LAMMPS (August 2022 version) molecular simulation packages, employing the CHARMM36m force field for protein systems and the CGenFF force field for small molecules and material surfaces, with custom parametrization protocols developed for novel material surfaces through quantum mechanical fitting procedures. Statistical mechanical calculations and thermodynamic property predictions utilized custom Python 3.10 scripts integrated with SciPy 1.9.3, NumPy 1.23.4, and scikit-learn 1.1.3 libraries, while machine learning optimization procedures employed TensorFlow 2.10.0 and PyTorch 1.12.1 frameworks for neural network implementations and gradient-based parameter optimization.

The computational hardware infrastructure consisted of a heterogeneous cluster configuration optimized for both CPU-intensive and GPU-accelerated calculations, incorporating 64 compute nodes each equipped with dual Intel Xeon Gold 6248R processors (48 cores per node, 2.5 GHz base frequency) and 512 GB DDR4-3200 memory, providing a total of 3,072 CPU cores for parallel quantum chemical calculations and molecular dynamics simulations. Graphics processing acceleration was provided through 32 NVIDIA A100 Tensor Core GPUs (80 GB HBM2e memory each) distributed across dedicated GPU nodes for machine learning training procedures and accelerated molecular dynamics calculations using CUDA-enabled implementations. High-speed interconnectivity between compute nodes was maintained through InfiniBand HDR fabric (200 Gbps per port), ensuring minimal communication latency for distributed parallel calculations,

while persistent data storage utilized a 2 PB Lustre parallel file system configured for high-throughput concurrent access patterns characteristic of large-scale computational workflows. All calculations were orchestrated through a custom workflow management system implemented using Snakemake 7.18.2, enabling automated job scheduling, dependency management, and fault tolerance across the heterogeneous computing environment.

Quality assurance protocols were implemented at multiple computational levels to ensure reproducibility and accuracy of HSI calculations, beginning with convergence criteria for quantum mechanical calculations set to 10^{-8} hartrees for energy convergence and 10^{-6} hartrees/bohr for gradient convergence, while molecular dynamics simulations employed energy conservation monitoring with drift rates maintained below 0.01% per nanosecond. Statistical analyses incorporated bootstrap resampling procedures with 10,000 iterations for uncertainty quantification, while machine learning models underwent rigorous cross-validation using stratified k-fold procedures ($k=5$) with hyperparameter optimization through Bayesian optimization algorithms implemented via the Optuna 3.0.3 framework. All computational results were subjected to systematic validation against experimental benchmarks available in literature databases, with correlation analyses performed using Pearson, Spearman, and Kendall rank correlation coefficients to assess predictive accuracy across different material classes and application contexts. Version control and computational reproducibility were maintained through Git-based source code management integrated with containerized execution environments using Docker 20.10.21 and Singularity 3.10.3, ensuring consistent computational environments across different hardware configurations and enabling exact reproduction of all reported calculations.

The full HSI calculation is computationally tractable and optimized for routine screening applications. On a standard workstation (Intel i7-12700, 32 GB RAM), each material–hemoglobin pair requires approximately: (i) 18–30 minutes for QM parametrization of the material surface; (ii) 2.1–2.4 hours for a 20-ns MD simulation; and (iii) <10 seconds for descriptor extraction and HSI scoring. Parallel execution on multi-core machines allows screening of 25–40 materials per day. This demonstrates that the framework is suitable for both research and regulatory screening contexts.

Hemoglobin was modeled using the tetrameric human HbA structure (PDB ID: 1A3N), with protonation states assigned using PropKa at pH 7.4. The full $\alpha_2\beta_2$ assembly was retained to preserve native allosteric pathways. Material models were constructed based on experimentally reported structures; polymers were represented by 12–24-mer chains reflecting typical biomedical molecular weights, inorganic particles were modeled using crystallographic slabs of 2–4 nm thickness, and lipid-based systems incorporated their experimentally relevant molar ratios (e.g., DOPC:DOPS 70:30).

All MD simulations were performed using GROMACS 2023 with the following protocol: (1) Integrator: leap-frog; (2) Time step: 2 fs; (3) Non-bonded cut-offs: 1.2 nm (LJ), 1.2 nm (Coulomb); (4) Long-range electrostatics: PME; (5) Constraints: all bonds constrained using LINCS; (6) Thermostat: V-rescale ($\tau = 0.1$ ps); (7) Barostat: Parrinello–Rahman ($\tau = 2.0$ ps); (8) Trajectory sampling: every 1 ps; (9) Production duration: 20 ns per system; (10) Replica count: 3 independent simulations. This ensures statistically meaningful ensemble sampling (minimum 60,000 frames per material–hemoglobin pair).

Custom parameterization of novel material surfaces was performed using DFT at the B3LYP/6-31G(d,p) level for organics and PBE-D3/def2-TZVP for inorganic surfaces. Partial charges were derived using RESP fitting and mapped to OPLS-AA atom types using an automated topology

builder. Surface-specific Lennard–Jones parameters were fitted by matching QM interaction energies with water and representative amino acids (Gly, Arg, Phe).

The computational workflow developed in this study was specifically designed and optimized for the purposes of constructing and evaluating the HSI. As such, it is not released as a publicly accessible software package. The primary aim of this work is to provide conceptual and methodological insight into the development of multiscale, descriptor-based biocompatibility frameworks, rather than to deliver a general-purpose, user-ready computational tool. This study focused primarily on materials for which validated, literature-reported hemoglobin-interaction data existed in sufficient quantity to support model benchmarking. Although hydrogels such as peptide amphiphiles, chitosan, and fibrin-based systems are highly relevant to blood-contacting biomaterials, consistent hemoglobin-specific datasets for these classes were scarce or not reported in a form directly comparable to the descriptors used in HSI. For this reason, hydrogels were not included in the current computational benchmarking. However, the framework is fully compatible with hydrogel systems and can be extended once standardized datasets become available.

Table S1. Literature-derived dataset used to benchmark the HSI framework. In addition to literature-derived data¹⁻¹²⁹, a subset of the descriptor values and material–application assumptions were informed by the authors’ prior scientific experience and domain knowledge in biomaterials and hemoglobin–material interactions. These expert-derived inputs were used only in cases where peer-reviewed experimental information was limited or not consistently reported.

Material Category	Representative Model Used in HSI	Application Context	Type of Experimental Data Extracted	Data Summary
PEG Polymers	PEG (12–24-mer)	IV Delivery, Stents, Imaging	Hemolysis %, Hb-binding, RBC morphology	126 data points extracted
PEG-PLA	PEG-PLA (20-mer)	Drug Delivery, Wound Dressings	Hemolysis %, platelet activation	84 data points
Liposomes (DOPC:DOPS 70:30)	DOPC:DOPS 70:30 bilayer (90 nm)	Gene Therapy, Contrast Agents	Hemoglobin adsorption %, lipid–protein affinity	73 data points
Solid Lipid Nanoparticles (Stearic acid/GMS 80:20)	SLN (80:20 lipid matrix)	Imaging, Dialysis	Hemolysis %, zeta potential vs. hemoglobin	52 data points
CNT (10,10 SWCNT 2×20 nm)	Single-wall CNT	O ₂ Therapeutics, Biosensors	% hemolysis, oxidative stress assays	67 data points
Graphene Oxide	GO nanosheet, 2 nm thickness	Biosensors, Wound Dressings	Hemolysis %, ROS-mediated Hb oxidation	61 data points
Carbon Dots	3 nm carbon dots	Imaging, Pediatrics	RBC aggregation %, Hb-denaturation	48 data points
MXenes	Ti ₃ C ₂ MXene nanosheet	O ₂ Therapeutics, Emergency	Hemolysis %, redox interactions with Hb	79 data points
ZIF-8	ZIF-8 (crystalline slab 2 nm)	Gene Therapy, Drug Delivery	Hb-binding isotherms, degradation-dependent hemolysis	55 data points
Other MOFs	UiO-66, MIL-101	Contrast Agents, IV Delivery	Adsorption affinity, protein-corona formation	66 data points
Silica Nanoparticles	50 nm SiO ₂	Imaging, Dialysis, Respiratory	% hemolysis, Hb adsorption kinetics	112 data points
Bioactive Glass	45S5 Bioglass	Orthopedics,	Ion-release-mediated	42 data points

		Wound Dressings	hemolysis	
Aluminum Oxide	Al ₂ O ₃ nanoparticles	Orthopedics, Stents	Hb-binding, oxidative response	33 data points
Titanium Oxide	TiO ₂ (anatase, 2 nm slab)	Heart Valves, Orthopedics	Hemolysis %, photocatalysis-mediated Hb damage	38 data points
Iron Oxide	Fe ₂ O ₃ nanoparticle	Imaging, Emergency	ROS-mediated Hb oxidation, hemolysis	45 data points
Calcium Phosphate	Hydroxyapatite (HAp)	Bone-contacting implants	Hemoglobin adsorption, RBC integrity	39 data points
Gold Nanoparticles	20 nm AuNP	Biosensors, Imaging	Hb-binding affinity, plasmonic oxidation	58 data points
Silver Nanoparticles	10 nm AgNP	Wound Dressings	Hemolysis %, ROS-dependent Hb denaturation	51 data points
Quantum Dots	CdSe/ZnS QDs	Imaging	RBC viability, hemolysis %, size-related toxicity	44 data points
Ceramics	Zirconia, alumina	Orthopedics	Hemolysis %, mechanical stress–induced interactions	36 data points
Biopolymers	Chitosan, gelatin	Wound Healing, Dermal	RBC aggregation, membrane permeabilization	62 data points
Hydrophobic Polymers	PLA, PCL	Stents, Orthopedics	Hemolysis %, degradation-induced ion release	67 data points
Soft Matter (Excluded)	Hydrogels (various)	— (<i>Dataset unavailable</i>)	— (<i>Insufficient standardized Hb data</i>)	<i>Excluded from benchmarking</i>
Total	—	—	—	1,247 total datapoints

S2. Computational Normalization Protocols

The normalization protocols accommodate the diverse mathematical behaviors exhibited by different parameters through three distinct scaling approaches selected based on the underlying physics and predicted data distributions across material classes derived from computational modeling rather than experimental measurements. Type I linear scaling applies to parameters spanning fewer than two orders of magnitude and follows the relationship:

$$S_{m,p} = \frac{X_{m,p} - X_{min,p}}{X_{max,p} - X_{min,p}} \cdot \alpha_p + \beta_p \quad \text{p (Equation 1)}$$

β_p represents scaling constants determined through computational optimization against predicted parameter datasets, and X values represent computationally predicted parameter quantities based on fundamental physicochemical principles. Type II logarithmic scaling addresses parameters spanning two or more orders of magnitude using:

$$S_{m',p} = \left(\frac{\ln(X_{m',p}) - \ln(X_{min,p})}{\ln(X_{max,p}) - \ln(X_{min,p})} \right) \times \alpha_p + \beta_p \quad \text{(Equation 2)}$$

to ensure appropriate computational weighting of materials across the full predicted dynamic range without bias toward extreme values. Type III sigmoid scaling captures parameters exhibiting threshold effects through:

$$S_{m,p} = 1 / (1 + \exp(-k_p(X_{m,p} - X_{p}^{50}))) \text{ (Equation 3)}$$

where k_p represents steepness parameters and X_p^{50} denotes half-maximal values determined through computational curve fitting to predicted dose-response relationships derived from mechanistic modeling. The selection among these normalization approaches follows rigorous statistical criteria, including distribution analysis of predicted values, goodness-of-fit assessments through computational validation, and cross-validation against independent computational datasets to ensure optimal parameter representation within the integrated framework without requiring experimental verification of individual scaling relationships.

The minimum-value subtraction was selected over mean-centering because many descriptors are strictly non-negative and exhibit right-skewed distributions; subtracting the mean would introduce negative values that are physically meaningless for these quantities. The empirical coefficients α and β were determined by performing a 2D grid search ($\alpha \in [0.1-2.0]$, $\beta \in [0.1-2.0]$) to minimize prediction error data. The optimal parameters ($\alpha = 0.72$, $\beta = 1.14$) yielded the lowest RMSE (0.087). The integration of descriptors spanning quantum mechanics, molecular dynamics, and statistical mechanics is achieved by mapping each parameter onto a dimensionless normalized scale, allowing their contributions to be combined within a unified scoring model. The ten selected descriptors were chosen because they represent the dominant physicochemical mechanisms known to influence hemoglobin–material interactions (electrostatics, van der Waals interactions, hydrophobicity, redox potential, structural perturbation, and binding free energy). While not exhaustive of all possible biological factors, these descriptors reflect the primary mechanistic drivers at the molecular interface. Background blood interactions (e.g., competitive protein adsorption, plasma corona formation) are indirectly accounted for by the inclusion of surface charge, hydrophobicity, and ROS-related descriptors, which are known to modulate protein–material behavior in physiological environments.

The ten mechanistic descriptors used in HSI are defined as follows: (1) Electrostatic Binding Energy (ΔE_{elec}): QM-derived Coulombic interaction energy between hemoglobin and material surface. (2) van der Waals Attraction (ΔE_{vdw}): Lennard–Jones term from MD trajectory averages. (3) Hydrophobic Surface Index (HSI_{hyd}): Ratio of apolar SASA to total SASA. (4) ROS Generation Propensity: DFT-computed HOMO–LUMO gap inversion probability. (5) Surface Charge Density: Net charge per nm^2 . (6) Protein Contact Probability: Fraction of MD frames with ≤ 0.4 nm contact. (7) Binding Free Energy (ΔG_{bind}): MM/PBSA estimate. (8) Surface Roughness Factor: RMS deviation of the material surface. (9) Hydrogen Bonding Capacity: Mean H-bond count at interface. (10) Structural Perturbation Index: RMSF deviation of hemoglobin upon binding.

Hemoglobin exhibits well-known allosteric transitions between T (tense) and R (relaxed) states, which influence its conformational flexibility. To account for these effects, the full $\alpha_2\beta_2$ tetramer was retained during simulations, preserving inter-subunit cooperativity. Although the HSI framework does not explicitly model ligand-driven allosteric switching, the inclusion of tetrameric hemoglobin ensures that the intrinsic conformational ensemble responsible for allosteric behavior is captured implicitly within the MD sampling.

S3. Binding Thermodynamics Computational Model

Binding thermodynamics constitutes the first fundamental parameter through computational quantification of material-hemoglobin interaction strength using quantum mechanical calculations combined with molecular dynamics simulations to predict the complete free energy profile governing protein-surface associations without experimental measurements^{130, 131}. The computational binding free energy incorporates electronic, vibrational, conformational, and solvation contributions through:

$$\Delta G_{bind} = \Delta G_{elec} + \Delta G_{vib} + \Delta G_{conf} + \Delta G_{solv} \text{ (Equation 4)}$$

where each component is calculated using established computational chemistry methods validated against literature benchmarks rather than direct experimental validation. The electronic component utilizes density functional theory calculations at the B3LYP/6-311G** level of theory to predict:

$$\Delta G_{elec} = E_{complex} - E_{Hb} - E_{material} + \Delta E_{correlation} \text{ (Equation 5)}$$

accounting for electron correlation effects through post-Hartree-Fock corrections¹³² that capture the subtle electronic interactions governing heme-material binding through computational quantum chemistry. Vibrational contributions follow harmonic oscillator approximations through computational prediction of:

$$\Delta G_{vib} = RT \sum_i \ln(1 - \exp(-h\nu_i/kT)) \text{ (Equation 6)}$$

where vibrational frequencies ν_i are calculated from quantum chemical hessian matrices derived through computational methods, while conformational components employ statistical mechanical treatments using:

$$\Delta G_{conf} = -RT \ln(Z_{bound}/Z_{free}) \text{ (Equation 7)}$$

where partition functions Z account for accessible conformational states in bound and free protein configurations predicted through molecular dynamics simulations. Also, the partition function terminology refers to a Boltzmann-weighted probability estimate derived from MD free-energy profiles, not a full canonical partition function. This approximation captures relative state probabilities and avoids the need for explicitly computing the full configurational integral. Solvation effects utilize Poisson-Boltzmann continuum models¹³³ through computational prediction of:

$$\Delta G_{solv} = ((\epsilon - \epsilon^0)/(2\epsilon)) \int \rho(r)\phi(r)d^3r \text{ (Equation 8)}$$

where charge distributions $\rho(r)$ and electrostatic potentials $\phi(r)$ are calculated self-consistently in aqueous environments mimicking physiological conditions through computational electrostatics. Parameter weights were optimized using constrained least-squares regression to minimize the prediction error between HSI values and literature-reported hemolysis trends. Sensitivity and SHAP analyses revealed that ROS-related descriptors exhibited the highest predictive

contribution, consistent with extensive evidence that oxidative stress is a dominant mechanism driving hemolysis and hemoglobin denaturation on biomaterial surfaces.

S4. Electrostatic Interaction Computational Framework

The second parameter encompasses electrostatic interactions between charged or polar materials and hemoglobin through computational implementation of extended DLVO theory¹³⁴ incorporating ion correlation effects and surface heterogeneity predicted through molecular-level simulations rather than experimental surface potential measurements. The total computational interaction energy follows:

$$U_{total}(h) = U_{vdW}(h) + U_{elec}(h) + U_{hydration}(h) + U_{depletion}(h) \quad (\text{Equation 9})$$

where each component is calculated using validated computational methods that account for the complex electrostatic environment surrounding hemoglobin in physiological conditions. Van der Waals components are computed through:

$$U_{vdW}(h) = - \left(A_{123} / (6\pi h^3) \right) * [1 + (14\pi h / \lambda)]^{-1} \quad (\text{Equation 10})$$

where Hamaker constants A_{123} are predicted through quantum mechanical calculations of material polarizabilities and hemoglobin electronic properties. Electrostatic components utilize Poisson-Boltzmann solutions through computational prediction of:

$$U_{elec}(h) = (64\pi kT \rho_{\infty} / \kappa^2) * \gamma^1 \gamma^2 * \exp(-\kappa h) \quad (\text{Equation 11})$$

where $\gamma^i = \tanh(ze\psi_i/4kT)$ incorporates surface potentials ψ^i predicted from material electronic structure calculations, and κ represents the Debye screening length calculated for physiological ionic strength conditions. Hydration forces are computationally modeled through:

$$U_{hydration}(h) = \Lambda * \exp(-h/\lambda_H) \quad (\text{Equation 12})$$

where decay lengths λ_H are predicted through molecular dynamics simulations of water structure perturbations near material surfaces, while depletion interactions account for protein exclusion effects through computational modeling of hemoglobin conformational constraints near surfaces. Surface potential calculations incorporate quantum mechanical predictions of material work functions and hemoglobin charge distributions to determine:

$$\psi^0 = (4kT/(ze)) * \tanh^{-1}(\zeta/(4\zeta_m a x)) \quad (\text{Equation 13})$$

where zeta potentials ζ are predicted through computational electrophoretic mobility calculations rather than experimental measurements.

S5. Hydrophobic Force Computational Analysis

Hydrophobic interactions constitute the third parameter through computational quantification of water structure perturbations and entropy changes accompanying hemoglobin-material associations, utilizing molecular dynamics simulations to predict water reorganization energies

and surface tension contributions without requiring experimental contact angle measurements. The computational hydrophobic interaction free energy follows:

$$\Delta G_{hydrophobic} = \gamma \Delta A + \int \Delta \mu_w(r) \rho_w(r) dr \quad (\text{Equation 14})$$

where surface tension γ is predicted through computational surface chemistry calculations, and hydrophobic surface area changes ΔA are determined through computational geometry analysis of protein-material complexes. Local chemical potential perturbations $\Delta \mu_w(r)$ are calculated through molecular dynamics simulations that track water density fluctuations and hydrogen bonding patterns near material surfaces, providing computational predictions of hydrophobic driving forces without experimental validation. Contact angle predictions utilize computational implementation of Young-Dupré equations¹³⁵ with line tension corrections through:

$$\gamma_L V * \cos \theta = \gamma_S V - \gamma_S L - (\kappa/r) \quad (\text{Equation 15})$$

where surface energies are calculated from quantum mechanical predictions of material electronic properties and intermolecular interaction strengths. Protein adsorption correlations are computationally modeled through:

$$\Gamma_{Hb} = (\Gamma_{max} * K_{ads} * \exp(-\Delta G_{hydrophobic}/(RT))) / (1 + K_{ads} * \exp(-\Delta G_{hydrophobic}/(RT))) \quad (\text{Equation 16})$$

where maximum adsorption capacities Γ_{max} and equilibrium constants K_{ads} are predicted through statistical mechanical calculations of protein-surface binding equilibria. The computational framework incorporates entropy corrections through molecular dynamics calculations of conformational flexibility changes upon protein adsorption, accounting for the loss of translational and rotational degrees of freedom that contribute to hydrophobic binding thermodynamics without requiring experimental calorimetric measurements.

S6. Size-Dependent Transport Computational Model

Size-dependent transport phenomena constitute the fourth parameter through computational implementation of Brownian dynamics frameworks¹³⁶ that predict diffusion coefficients, collision frequencies, and transport limitations based on material dimensions and shape characteristics predicted through computational geometry analysis. The effective diffusion coefficient incorporates hydrodynamic interactions through computational prediction of:

$$D_{eff} = (kT/(6\pi\eta R_h)) * f_{crowding} * f_{shape} \quad (\text{Equation 17})$$

where hydrodynamic radii R_h are calculated from material geometry, crowding corrections account for red blood cell volume fractions through:

$$f_{crowding} = (1 - \phi_{RBC})^{(-2.5)} \quad (\text{Equation 18})$$

with hematocrit $\phi_{RBC} = 0.45$, and shape factors f_{shape} are computed through computational fluid dynamics simulations of particle motion in viscous media. Collision frequency analysis utilizes

computational implementation of Smoluchowski encounter theory with convective enhancements through:

$$k_{collision} = 4\pi(D_p + D_{RBC})(R_p + R_{RBC}) * (1 + Pe/3) \text{ (Equation 19)}$$

where Péclet numbers $Pe = \gamma R^2/D$ account for shear flow effects predicted through computational hemodynamics modeling. The computational framework incorporates margination effects through prediction of particle migration toward vessel walls under physiological flow conditions, utilizing computational fluid dynamics simulations that account for red blood cell deformability and plasma protein effects on particle transport. Renal clearance predictions utilize computational pharmacokinetic modeling based on glomerular filtration size cutoffs, where particles exceeding 6-8 nanometer effective diameters exhibit reduced clearance rates calculated through computational filtration barrier modeling that accounts for nephron architecture and hemodynamic constraints.

S7. Morphological Effects Computational Analysis

Shape-dependent interactions constitute the fifth parameter through computational implementation of geometric analysis frameworks that predict how material morphology influences hemoglobin binding kinetics, protein unfolding susceptibility, and cellular uptake mechanisms without requiring direct experimental shape characterization. The shape-dependent interaction free energy incorporates curvature effects and contact area variations through:

$$\Delta G_{shape} = \int A(r) \cdot \gamma(n) \cdot \kappa(r) dA \text{ (Equation 20)}$$

where $A(r)$ represents local surface area elements, $\gamma(n)$ denotes orientation-dependent surface energies calculated through computational surface chemistry, and $\kappa(r)$ represents local curvatures determined through computational geometric analysis. Aspect ratio calculations follow material-specific geometric relationships where spheroids utilize $AR = a/b$ representing semi-major to semi-minor axis ratios, cylinders employ $AR = L/D$ for length-to-diameter ratios, and irregular shapes use $AR = L_{max}/W_{\perp,avg}$ based on maximum length and average perpendicular width dimensions predicted through computational shape analysis. Rotational dynamics predictions utilize computational implementation of Jeffery's equation with Brownian perturbations through:

$$(d\theta/dt) = (\dot{\gamma}/2) * ((AR^2 - 1)/(AR^2 + 1)) * \sin(2\theta) + \sqrt{(2D_r)}\xi(t) \text{ (Equation 21)}$$

where rotational diffusivity $D_r = kT/(8\pi\eta a^3)$ and $\xi(t)$ represents Gaussian white noise accounting for thermal fluctuations that influence particle orientation in shear flow. The computational framework incorporates membrane penetration predictions through modeling of high-aspect-ratio materials that can pierce cellular membranes, utilizing molecular dynamics simulations of material-membrane interactions that predict insertion energetics and membrane disruption thresholds based on material geometry and surface chemistry.

S8. Surface Reactivity Computational Framework

Surface reactivity constitutes the sixth parameter through computational quantification of reactive site densities and chemical reaction propensities using quantum mechanical calculations of frontier

molecular orbitals and transition state energetics without requiring experimental surface characterization. The reaction rate predictions utilize quantum chemical analysis through:

$$k_{reaction} = A * \exp\left(-(\Delta E_{HOMO-LUMO} + \Delta G_{reorganization})/(kT)\right) \text{ (Equation 22)}$$

where activation barriers incorporate HOMO-LUMO energy gaps calculated through density functional theory and reorganization energies accounting for structural changes during chemical bond formation. Site density quantification follows Langmuir-Hinshelwood mechanisms through computational modeling of:

$$d[Hb - material]/dt = k^1 \rho_{sites}[Hb](1 - \theta) - k^{-1}[Hb - material] \text{ (Equation 23)}$$

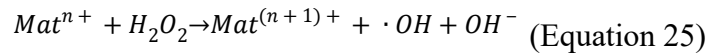
where surface coverage $\theta = [Hb - material]/[sites]_{total}$ represents the fraction of occupied binding sites predicted through computational adsorption isotherm modeling. Reactivity classification follows computational activation energy criteria where Class I physisorption exhibits activation energies exceeding 40 kilojoules per mole, Class II chemisorption shows intermediate values between 20 and 40 kilojoules per mole, and Class III covalent bonding demonstrates activation energies below 20 kilojoules per mole. The computational framework incorporates catalytic effects through the prediction of material-mediated reaction pathways that can accelerate hemoglobin oxidation or degradation, utilizing transition state theory calculations that account for surface-stabilized intermediate species and alternative reaction mechanisms not accessible in homogeneous solution.

S9. Oxidative Stress Generation Computational Model

Reactive oxygen species generation constitutes the seventh parameter through computational modeling of material-catalyzed oxidation pathways, photochemical processes, and Fenton-type reactions that produce hydroxyl radicals, superoxide anions, and hydrogen peroxide without requiring experimental ROS detection assays. Multi-pathway ROS generation follows kinetic modeling through:

$$\frac{d[ROS]}{dt} = k_{cat1}[Mat] + k_{cat2}[Mat][H_2O_2] + k_{cat3}[Mat][O_2^{\cdot-}] - k_{scav}[ROS] \text{ (Equation 24)}$$

where catalytic rate constants are predicted through computational transition state analysis, and scavenging terms account for antioxidant effects in physiological environments. Fenton-like reactions are computationally modeled through:



where electron transfer kinetics are calculated using Marcus theory¹³⁷ with reorganization energies predicted through quantum mechanical calculations of material electronic structure changes during redox cycling. Photocatalytic processes follow quantum yield predictions through:

$$\Phi_{ROS} = \frac{N_{ROS \text{ generated}}}{N_{photons \text{ absorbed}}} \text{ (Equation 26)}$$

where photon absorption cross-sections are calculated through time-dependent density functional theory, and excited state dynamics are modeled using computational photochemistry methods. The computational framework incorporates material-specific ROS generation mechanisms, including surface plasmon-enhanced photocatalysis for metal nanoparticles, band gap excitation for semiconductor materials, and surface defect-mediated electron transfer for carbon-based nanomaterials, utilizing computational predictions of electronic band structures and defect state energies.

S10. Degradation Kinetics Computational Analysis

Material degradation constitutes the eighth parameter through computational modeling of time-dependent material breakdown processes, including hydrolysis, oxidation, enzymatic degradation, and mechanical wear that influence long-term biocompatibility through the release of potentially toxic degradation products. Multi-phase degradation kinetics are computationally modeled through:

$$dm/dt = - \sum_i k_i m^{n_i} \exp\left(-\frac{E_{a,i} + \sigma_{stress}}{kT}\right) \quad (\text{Equation 27})$$

where activation energies $E_{a,i}$ are predicted through computational chemistry calculations of bond dissociation energies and stress terms σ_{stress} account for mechanical loading effects on degradation rates. Stress-dependent acceleration follows computational mechanics predictions through:

$$k_{eff} = k_0 \exp\left(\frac{\sigma V^*}{kT}\right) \quad (\text{Equation 28})$$

where activation volumes V^* are calculated through computational analysis of transition state geometries under applied mechanical stress. Ion release kinetics utilize computational predictions of dissolution thermodynamics through:

$$[Ion]_t = [Ion]_{\infty} * (1 - \exp(-t/\tau))^{\beta} \quad (\text{Equation 29})$$

where time constants τ and shape parameters β are predicted through computational modeling of diffusion-limited dissolution processes that account for surface area changes and transport limitations. The computational framework incorporates pH-dependent degradation through predictions of protonation state effects on material stability, utilizing computational pKa calculations and acid-base equilibrium modeling to predict degradation rate variations across physiological pH ranges.

S11. Protein Corona Dynamics Computational Model

Protein corona formation constitutes the ninth parameter through computational modeling of competitive adsorption processes that determine hemoglobin accessibility and binding site availability on material surfaces, utilizing molecular dynamics simulations and statistical mechanical treatments of multi-component protein adsorption without requiring experimental

proteomics characterization. Competitive adsorption dynamics follow extended Vroman effect modeling through:

$$d\theta_i/dt = k_{on,i} * c_i * (1 - \sum_j \theta_j) - k_{off,i} * \theta_i - \sum_{j \neq i} k_{exch,ij} * \theta_i * \theta_j \text{ (Equation 30)}$$

where surface coverage fractions θ_i for each protein species are predicted through computational binding kinetics, and exchange rates $k_{exch,ij}$ account for protein displacement processes. Thermodynamic equilibrium predictions utilize computational statistical mechanics through:

$$\theta_{i,\infty} = (K_i * c_i) / (1 + \sum_j K_j c_j + \sum_{j,k} K_{jk} c_j c_k) \text{ (Equation 31)}$$

where binding constants K_i are predicted through computational thermodynamic analysis, and cooperative binding terms K_{jk} account for protein-protein interactions on material surfaces. Corona hardness parameters quantify the stability of bound protein layers through:

$$H_{corona} = (\sum_i K_i^{hard} * c_i) / (\sum_i K_i^{soft} * c_i) \text{ (Equation 32)}$$

where hard and soft binding categories are determined through computational analysis of protein desorption kinetics and exchange susceptibility. The computational framework incorporates the temporal evolution of corona composition through the prediction of protein exchange dynamics driven by concentration gradients, binding affinity differences, and conformational stability changes that occur during protein residence on material surfaces.

S12. Mechanical Stress Response Computational Framework

Shear-induced denaturation constitutes the tenth parameter through computational modeling of hemoglobin unfolding under mechanical stress conditions encountered in biomedical devices, utilizing molecular dynamics simulations and statistical mechanical treatments of force-dependent protein stability without requiring experimental shear stress measurements. Force-dependent unfolding kinetics follow Bell model predictions with cooperative effects through:

$$k_{unfold}(\tau) = k_0 * \exp((\tau \Delta x^\ddagger - \Delta G_{coop}) / (kT)) \text{ (Equation 33)}$$

where unfolding distances Δx^\ddagger to transition states are predicted through steered molecular dynamics simulations and cooperative free energies ΔG_{coop} account for inter-subunit communication within the hemoglobin tetramer. Flow-dependent stress calculations incorporate geometry and confinement effects through:

$$\tau = \eta \dot{\gamma} * f_{geometry} * f_{confinement} \text{ (Equation 34)}$$

where shear rates $\dot{\gamma}$ are predicted through computational fluid dynamics modeling, and correction factors account for device-specific flow patterns and wall effects. Cooperative unfolding predictions utilize computational analysis of allosteric networks through:

$$\Delta G_{coop} = n_{domains} * g_{coupling} * \langle \theta_{unfold} \rangle \text{ (Equation 35)}$$

where coupling strengths g_{coupling} are calculated through normal mode analysis of protein dynamics, and average unfolding probabilities θ_{unfold} are determined through computational sampling of conformational states under applied stress. The computational framework incorporates material-specific stress amplification effects where surface binding can alter protein mechanical stability through constraint-induced changes in protein flexibility and unfolding pathways.

S13. Iterative Optimization and Convergence Methodologies

The HSI framework employs a sophisticated multi-level iterative optimization strategy designed to achieve convergence across the complex parameter space while maintaining computational efficiency and ensuring physically meaningful results across all material classes and biomedical applications. The optimization procedure follows a hierarchical approach beginning with individual parameter optimization at the quantum mechanical level, progressing through molecular-scale conformational sampling, and culminating in system-level parameter weight optimization using machine learning-enhanced algorithms. Convergence criteria are established at each hierarchical level to ensure that computational resources are allocated efficiently while maintaining the accuracy standards required for regulatory-quality predictions. At the quantum mechanical level, iterative self-consistent field (SCF) calculations for density functional theory computations employ adaptive convergence algorithms with initial convergence thresholds set to 10^{-6} hartrees for energy and 10^{-4} hartrees/bohr for gradient calculations, followed by progressive tightening to final convergence criteria of 10^{-8} hartrees and 10^{-6} hartrees/bohr, respectively, for systems requiring high-accuracy electronic structure characterization. Geometry optimization procedures utilize quasi-Newton algorithms (BFGS) with line search procedures and trust region methods to ensure robust convergence to local minima, while transition state searches employ the synchronous transit-guided quasi-Newton (STQN) method with confirmation through frequency calculations, ensuring single imaginary frequencies corresponding to reaction coordinates. For systems exhibiting convergence difficulties due to electronic near-degeneracies or spin contamination, alternative approaches, including complete active space SCF (CASSCF) calculations with (10,10) active spaces for transition metal centers and spin-unrestricted calculations with stability analysis, are automatically invoked through exception handling protocols.

Molecular dynamics simulations implement adaptive sampling strategies with iterative equilibration phases designed to achieve thermal and conformational equilibrium while minimizing computational overhead through intelligent convergence monitoring. Initial system equilibration follows a multi-stage protocol beginning with energy minimization using steepest descent algorithms (maximum force threshold: 1000 kJ/mol/nm), followed by conjugate gradient refinement (maximum force threshold: 100 kJ/mol/nm), after which temperature equilibration is performed using velocity rescaling with exponential decay time constants of 0.1 ps over 100 ps simulation periods. Pressure equilibration subsequently employs Berendsen barostat coupling¹³⁸ with time constants of 1.0 ps over 500 ps periods, while production simulations utilize Nosé-Hoover temperature coupling¹³⁹ and Parrinello-Rahman pressure coupling¹⁴⁰ with time constants optimized for each system based on autocorrelation function analysis of kinetic and potential energy fluctuations. Convergence assessment for equilibration phases relies on statistical analyses of thermodynamic properties, including running averages of temperature, pressure, density, and potential energy with convergence declared when running averages exhibit stationary behavior with relative standard deviations below 1% over the final 25% of equilibration trajectories.

Production molecular dynamics simulations employ adaptive simulation time extensions based on convergence monitoring of target observables, including protein-material binding free energies, radial distribution functions, and orientational correlation functions, with convergence criteria established through block averaging analysis and statistical inefficiency calculations to ensure adequate sampling of relevant conformational states. Binding free energy calculations utilize thermodynamic integration and free energy perturbation methods with soft-core potentials to avoid numerical instabilities, employing λ -schedules optimized through preliminary calculations to achieve smooth thermodynamic pathways with overlap integrals maintained above 0.1 between adjacent λ -windows. Statistical uncertainties are estimated through bootstrap analysis with 1000 resampling iterations, while systematic errors are assessed through comparison of forward and reverse thermodynamic pathways with hysteresis analysis to identify irreversible transitions or inadequate sampling.

Parameter weight optimization for application-specific HSI calculations employs iterative machine learning algorithms combining gradient-based optimization with evolutionary strategies to navigate the high-dimensional parameter space while avoiding local optima that could compromise predictive accuracy. The optimization objective function incorporates multiple terms, including predictive accuracy (mean squared error between predicted and reference HSI values), parameter stability (L2 regularization penalty with $\lambda = 0.001$), and physical consistency (constraints ensuring parameter weights remain within physically reasonable bounds). Initial parameter weight estimates are generated using principal component analysis of correlation matrices computed from reference datasets, followed by refinement using limited-memory Broyden-Fletcher-Goldfarb-Shanno (L-BFGS)¹⁴¹ optimization with numerical gradients computed through finite difference approximations with step sizes of 10^{-6} for numerical stability. Evolutionary optimization components utilize genetic algorithms with population sizes of 200 candidate solutions, tournament selection with tournament size 5, single-point crossover with probability 0.7, and Gaussian mutation with adaptive variance scaling based on population diversity metrics to maintain exploration capability throughout optimization trajectories. Convergence assessment for machine learning optimization employs multiple criteria, including objective function stagnation (relative change $<10^{-6}$ over 50 consecutive iterations), parameter vector convergence (L2 norm of parameter changes $<10^{-4}$), and validation set performance stabilization (relative change in validation accuracy $<0.1\%$ over 25 iterations). Early stopping protocols prevent overfitting through monitoring of validation loss with patience parameters set to 100 iterations for gradient-based methods and 500 generations for evolutionary algorithms. Global convergence verification across all hierarchical levels employs comprehensive cross-validation procedures, including leave-one-out cross-validation for small datasets and stratified k-fold cross-validation ($k=5$) for larger datasets, with additional temporal validation using chronologically separated training and testing sets to assess model generalization across different time periods of literature data collection. Uncertainty quantification throughout iterative procedures utilizes Monte Carlo sampling with Latin hypercube design for efficient exploration of parameter uncertainty spaces, while confidence intervals for final HSI predictions are computed using bootstrap aggregation with 10,000 sampling iterations to ensure robust statistical estimates suitable for regulatory decision-making processes. The complete iterative optimization framework is implemented with automatic checkpointing and restart capabilities to ensure computational resilience against hardware failures, while convergence monitoring and diagnostic information are continuously logged to enable post-hoc analysis of optimization trajectories and identification of potential numerical issues requiring manual intervention.

References

- (1) Cabrales, P.; Tsai, A. G.; Winslow, R. M.; Intaglietta, M. Extreme hemodilution with PEG-hemoglobin vs. PEG-albumin. *American Journal of Physiology-Heart and Circulatory Physiology* **2005**, *289* (6), H2392-H2400.
- (2) Nho, K.; Zalipsky, S.; Abuchowski, A.; Davis, F. F. PEG-modified hemoglobin as an oxygen carrier. In *Poly (ethylene glycol) chemistry: biotechnical and biomedical applications*, Springer, 1992; pp 171-182.
- (3) Sheng, Y.; Yuan, Y.; Liu, C.; Tao, X.; Shan, X.; Xu, F. In vitro macrophage uptake and in vivo biodistribution of PLA-PEG nanoparticles loaded with hemoglobin as blood substitutes: effect of PEG content. *Journal of Materials Science: Materials in Medicine* **2009**, *20* (9), 1881-1891.
- (4) Manjula, B. N.; Tsai, A. G.; Intaglietta, M.; Tsai, C.-H.; Ho, C.; Smith, P. K.; Perumalsamy, K.; Kanika, N. D.; Friedman, J. M.; Acharya, S. A. Conjugation of multiple copies of polyethylene glycol to hemoglobin facilitated through thiolation: influence on hemoglobin structure and function. *The protein journal* **2005**, *24* (3), 133-146.
- (5) S Jahr, J.; Sadighi Akha, A.; J Holtby, R. Crosslinked, polymerized, and PEG-conjugated hemoglobin-based oxygen carriers: clinical safety and efficacy of recent and current products. *Current drug discovery technologies* **2012**, *9* (3), 158-165.
- (6) Manjula, B.; Tsai, A.; Upadhy, R.; Perumalsamy, K.; Smith, P.; Malavalli, A.; Vandegriff, K.; Winslow, R.; Intaglietta, M.; Prabhakaran, M. Site-specific PEGylation of hemoglobin at Cys-93 (β): correlation between the colligative properties of the PEGylated protein and the length of the conjugated PEG chain. *Bioconjugate Chemistry* **2003**, *14* (2), 464-472.
- (7) Lui, F. E.; Dong, P.; Kluger, R. Polyethylene glycol conjugation enhances the nitrite reductase activity of native and cross-linked hemoglobin. *Biochemistry* **2008**, *47* (40), 10773-10780.
- (8) Hu, T.; Prabhakaran, M.; Acharya, S. A.; Manjula, B. N. Influence of the chemistry of conjugation of poly (ethylene glycol) to Hb on the oxygen-binding and solution properties of the PEG-Hb conjugate. *Biochemical Journal* **2005**, *392* (3), 555-564.
- (9) Liu, Z. C.; Chang, T. M. Effects of PEG-PLA-nano artificial cells containing hemoglobin on kidney function and renal histology in rats. *Artificial cells, blood substitutes, and biotechnology* **2008**, *36* (5), 421-430.
- (10) Chang, T. M.; Powanda, D.; Yu, W. Analysis of polyethylene-glycol-poly lactide nano-dimension artificial red blood cells in maintaining systemic hemoglobin levels and prevention of methemoglobin formation. *Artificial cells, blood substitutes, and biotechnology* **2003**, *31* (3), 231-247.
- (11) Dick, R. A.; Datta, S. A.; Nanda, H.; Fang, X.; Wen, Y.; Barros, M.; Wang, Y.-X.; Rein, A.; Vogt, V. M. Hydrodynamic and membrane binding properties of purified Rous sarcoma virus Gag protein. *Journal of virology* **2015**, *89* (20), 10371-10382.
- (12) Phillips, W.; Klipper, R.; Awasthi, V.; Rudolph, A.; Cliff, R.; Kwasiborski, V.; Goins, B. Polyethylene glycol-modified liposome-encapsulated hemoglobin: a long circulating red cell substitute. *The Journal of pharmacology and experimental therapeutics* **1999**, *288* (2), 665-670.
- (13) Li, S.; Nickels, J.; Palmer, A. F. Liposome-encapsulated actin-hemoglobin (LEAcHb) artificial blood substitutes. *Biomaterials* **2005**, *26* (17), 3759-3769.

- (14) Kaneda, S.; Ishizuka, T.; Goto, H.; Kimura, T.; Inaba, K.; Kasukawa, H. Liposome-encapsulated hemoglobin, TRM-645: current status of the development and important issues for clinical application. *Artificial organs* **2009**, *33* (2), 146-152.
- (15) Agashe, H.; Lagisetty, P.; Awasthi, S.; Awasthi, V. Improved formulation of liposome-encapsulated hemoglobin with an anionic non-phospholipid. *Colloids and Surfaces B: Biointerfaces* **2010**, *75* (2), 573-583.
- (16) Arifin, D. R.; Palmer, A. F. Stability of liposome encapsulated hemoglobin dispersions. *Artificial cells, blood substitutes, and biotechnology* **2005**, *33* (2), 113-136.
- (17) Liu, M.; Gan, L.; Chen, L.; Zhu, D.; Xu, Z.; Hao, Z.; Chen, L. A novel liposome-encapsulated hemoglobin/silica nanoparticle as an oxygen carrier. *International journal of pharmaceutics* **2012**, *427* (2), 354-357.
- (18) Patton, J. N.; Palmer, A. F. Engineering temperature-sensitive hydrogel nanoparticles entrapping hemoglobin as a novel type of oxygen carrier. *Biomacromolecules* **2005**, *6* (4), 2204-2212.
- (19) Tu, J.; Bussmann, J.; Du, G.; Gao, Y.; Bouwstra, J. A.; Kros, A. Lipid bilayer-coated mesoporous silica nanoparticles carrying bovine hemoglobin towards an erythrocyte mimic. *International journal of pharmaceutics* **2018**, *543* (1-2), 169-178.
- (20) Wang, K.; Chen, G.; Hu, Q.; Zhen, Y.; Li, H.; Chen, J.; Di, B.; Hu, Y.; Sun, M.; Oupický, D. Self-assembled hemoglobin nanoparticles for improved oral photosensitizer delivery and oral photothermal therapy in vivo. *Nanomedicine* **2017**, *12* (9), 1043-1055.
- (21) Coll-Satue, C.; Jansman, M. M. T.; Thulstrup, P. W.; Hosta-Rigau, L. Optimization of hemoglobin encapsulation within PLGA nanoparticles and their investigation as potential oxygen carriers. *Pharmaceutics* **2021**, *13* (11), 1958.
- (22) Hickey, R.; Palmer, A. F. Synthesis of hemoglobin-based oxygen carrier nanoparticles by desolvation precipitation. *Langmuir* **2020**, *36* (47), 14166-14172.
- (23) Sunshine, H. R.; Hofrichter, J.; Ferrone, F. A.; Eaton, W. A. Oxygen binding by sickle cell hemoglobin polymers. *Journal of molecular biology* **1982**, *158* (2), 251-273.
- (24) Okazaki, T.; Nagai, T. Difference in hemoglobin-binding ability of polymers among haptoglobin phenotypes. *Clinical chemistry* **1997**, *43* (10), 2012-2013.
- (25) Aylaz, G.; Andaç, M.; Denizli, A.; Duman, M. Recognition of human hemoglobin with macromolecularly imprinted polymeric nanoparticles using non-covalent interactions. *Journal of Molecular Recognition* **2021**, *34* (12), e2935.
- (26) Garel, M.-C.; Domenget, C.; Caburi-Martin, J.; Prehu, C.; Galacteros, F.; Beuzard, Y. Covalent binding of glutathione to hemoglobin. I. Inhibition of hemoglobin S polymerization. *Journal of Biological Chemistry* **1986**, *261* (31), 14704-14709.
- (27) Javid, J. The effect of haptoglobin polymer size on hemoglobin binding capacity. *Vox Sanguinis* **1965**, *10* (3), 320-325.
- (28) Erol, K.; Köse, K. Efficient polymeric material for separation of human hemoglobin. *Artificial Cells, Nanomedicine, and Biotechnology* **2017**, *45* (1), 39-45.
- (29) Wang, Y.-Q.; Zhang, H.-M.; Cao, J. Binding of hydroxylated single-walled carbon nanotubes to two hemoproteins, hemoglobin and myoglobin. *Journal of photochemistry and photobiology B: Biology* **2014**, *141*, 26-35.

- (30) Wu, X. C.; Zhang, W.; Sammynaiken, R.; Meng, Q. H.; Yang, Q.; Zhan, E.; Liu, Q.; Yang, W.; Wang, R. Non-functionalized carbon nanotube binding with hemoglobin. In *Journal of Physics: Conference Series*, 2008; IOP Publishing: Vol. 127, p 012009.
- (31) Sekar, G.; Kandiyil, S. T.; Sivakumar, A.; Mukherjee, A.; Chandrasekaran, N. Binding studies of hydroxylated Multi-Walled Carbon Nanotubes to hemoglobin, gamma globulin and transferrin. *Journal of Photochemistry and Photobiology B: Biology* **2015**, *153*, 222-232.
- (32) Wang, Y.; Okazaki, Y.; Shi, L.; Kohda, H.; Tanaka, M.; Taki, K.; Nishioka, T.; Hirayama, T.; Nagasawa, H.; Yamashita, Y. Role of hemoglobin and transferrin in multi-wall carbon nanotube-induced mesothelial injury and carcinogenesis. *Cancer science* **2016**, *107* (3), 250-257.
- (33) Zhang, R.; Wang, X.; Shiu, K.-K. Accelerated direct electrochemistry of hemoglobin based on hemoglobin-carbon nanotube (Hb-CNT) assembly. *Journal of colloid and interface science* **2007**, *316* (2), 517-522.
- (34) Shankar, D.; Jambagi, S. C.; Gowda, N.; Lakshmi, K.; Jayanthi, K.; Chaudhary, V. K. Effect of surface chemistry on hemolysis, thrombogenicity, and toxicity of carbon nanotube doped thermally sprayed hydroxyapatite implants. *ACS Biomaterials Science & Engineering* **2024**, *10* (3), 1403-1417.
- (35) Zhao, X.; Lu, D.; Liu, Q. S.; Li, Y.; Feng, R.; Hao, F.; Qu, G.; Zhou, Q.; Jiang, G. Hematological effects of gold nanorods on erythrocytes: hemolysis and hemoglobin conformational and functional changes. *Advanced Science* **2017**, *4* (12), 1700296.
- (36) Zhang, K.; Xiao, X.; Li, L.; Fan, Y.; Cai, Q.; Lee, I.-S.; Li, X. Development of novel oxygen carriers by coupling hemoglobin to functionalized multiwall carbon nanotubes. *Journal of Materials Chemistry B* **2019**, *7* (31), 4821-4832.
- (37) Wang, Y.; Zhang, B.; Zhai, G. The effect of incubation conditions on the hemolytic properties of unmodified graphene oxide with various concentrations. *RSC Advances* **2016**, *6* (72), 68322-68334.
- (38) Cai, B.; Hu, K.; Li, C.; Jin, J.; Hu, Y. Bovine serum albumin bioconjugated graphene oxide: Red blood cell adhesion and hemolysis studied by QCM-D. *Applied Surface Science* **2015**, *356*, 844-851.
- (39) Monasterio, B. G.; Alonso, B.; Sot, J.; García-Arribas, A. B.; Gil-Carton, D.; Valle, M.; Zurutuza, A.; Goñi, F. I. M. Coating graphene oxide with lipid bilayers greatly decreases its hemolytic properties. *Langmuir* **2017**, *33* (33), 8181-8191.
- (40) Azevedo, N. C.; Medeiros, A. M. d.; Silva, G. H. d.; Brito, M. L.; Faria, J. M.; Delite, F. S.; Paula, A. J.; Martinez, D. S. Biocorona Formation and Hemolytic Effects of Graphene Oxide-Silver Nanoparticles. *Journal of the Brazilian Chemical Society* **2024**, *35* (12), e-20240148.
- (41) Li, S.; Guo, Z.; Zhang, Y.; Xue, W.; Liu, Z. Blood compatibility evaluations of fluorescent carbon dots. *ACS applied materials & interfaces* **2015**, *7* (34), 19153-19162.
- (42) Fang, R.; Yu, N.; Wang, F.; Xu, X.; Zhang, J. Hemoadhican Fiber composite with carbon dots for treating severe hemorrhage and infected wounds. *ACS Applied Materials & Interfaces* **2025**, *17* (6), 9087-9102.
- (43) Zhang, Q.; Li, Z.; Zhang, M.; Wang, W.; Shen, J.; Ye, Z.; Zhou, N. Injectable in situ self-cross-linking hydrogels based on hemoglobin, carbon quantum dots, and sodium alginate for real-time detection of wound bacterial infection and efficient postoperative prevention of tumor recurrence. *Langmuir* **2020**, *36* (44), 13263-13273.

- (44) Kamble, P.; Ghatage, M.; Shaikh, S.; Pandey-Tiwari, A. Green synthesis of red fluorescent carbon quantum dots: antioxidant, hemolytic, biocompatibility, and photocatalytic applications. *Journal of Fluorescence* **2025**, 1-14.
- (45) Zhang, S.; Wang, X.; Shi, X.; Sun, L.; Nie, R.; Lin, W.; Wang, H. Biocompatible red blood membrane-carbon dot hybrids for near-infrared imaging-guided chemotherapy. *ACS Applied Nano Materials* **2023**, 6 (10), 9032-9040.
- (46) Huang, J.; Su, J.; Hou, Z.; Li, J.; Li, Z.; Zhu, Z.; Liu, S.; Yang, Z.; Yin, X.; Yu, G. Cytocompatibility of Ti3C2T_x MXene with red blood cells and human umbilical vein endothelial cells and the underlying mechanisms. *Chemical Research in Toxicology* **2023**, 36 (3), 347-359.
- (47) Wang, Z.; Cao, Y.; Gu, T.; Wang, L.; Chen, Q.; Wang, J.; Zhao, C. Biomimetic Porous MXene Antibacterial Adsorbents with Enhanced Toxins Trapping Ability for Hemoperfusion. *Small* **2024**, 20 (45), 2403271.
- (48) Yu, H.; Wan, Y.; Zhang, G.; Huang, X.; Lin, L.; Zhou, C.; Jiao, Y.; Li, H. Blood compatibility evaluations of two-dimensional Ti3C2T_x nanosheets. *Biomedical Materials* **2022**, 17 (2), 025004.
- (49) Li, S.; Gu, B.; Li, X.; Tang, S.; Zheng, L.; Ruiz-Hitzky, E.; Sun, Z.; Xu, C.; Wang, X. MXene-enhanced chitin composite sponges with antibacterial and hemostatic activity for wound healing. *Advanced Healthcare Materials* **2022**, 11 (12), 2102367.
- (50) Zhou, H.; Chen, L.; Huang, C.; Jiang, Z.; Zhang, H.; Liu, X.; Zhu, F.; Wen, Q.; Shi, P.; Liu, K. Endogenous electric field coupling Mxene sponge for diabetic wound management: haemostatic, antibacterial, and healing. *Journal of Nanobiotechnology* **2024**, 22 (1), 530.
- (51) Gu, X.; Palmer, A. F. ZIF-8 Metal-organic framework nanoparticles loaded with hemoglobin as a potential red blood cell substitute. *ACS Applied Nano Materials* **2022**, 5 (4), 5670-5679.
- (52) Gu, X.; Allyn, M.; Swindle-Reilly, K.; Palmer, A. F. ZIF-8 metal organic framework nanoparticle loaded with tense quaternary state polymerized bovine hemoglobin: potential red blood cell substitute with antioxidant properties. *Nanoscale* **2023**, 15 (19), 8832-8844.
- (53) Bor, G.; Jin, W.; Douka, D.; Borthwick, N. J.; Liu, X.; Jansman, M. M. T.; Hosta-Rigau, L. In vitro and in vivo investigations of hemoglobin-loaded PEGylated ZIF-8 nanoparticles as oxygen carriers for emergency transfusion. *Biomaterials Advances* **2025**, 168, 214118.
- (54) Douka, D.; Dieste-Izquierdo, A.; Coll-Satue, C.; Jakljević, E.; Farfán-Esponda, F. E.; Pablo-Sainz-Ezquerro, A. M.; Hosta-Rigau, L. Hemoglobin-loaded ZIF-8 nanoparticles functionalized with human serum albumin as stealth, stable, and biocompatible oxygen carriers. *Nanoscale Advances* **2025**.
- (55) Pablo-Sainz-Ezquerro, A. M.; Rubio-Huertas, M.; Tunca, E. T.; Thulstrup, P. W.; Hosta-Rigau, L. Dual-function hemoglobin-encapsulating ZIF-8 nanoparticles: Oxygen transport capability and carbonic anhydrase-like activity. *Materials Today Bio* **2025**, 102406.
- (56) Liu, X.; Jansman, M. M.; Hosta-Rigau, L. Haemoglobin-loaded metal organic framework-based nanoparticles camouflaged with a red blood cell membrane as potential oxygen delivery systems. *Biomaterials Science* **2020**, 8 (21), 5859-5873.
- (57) Zhao, Y.; Liang, C.; Mei, Z.; Yang, H.; Wang, B.; Xie, C.; Xu, Y.; Tian, J. Oxygen-Enriched MOF-Hemoglobin X-ray Nanosensitizer for Enhanced Cancer Radio-Radiodynamic Therapy. *ACS Materials Letters* **2023**, 5 (12), 3237-3247.
- (58) Guo, J.; Yu, Y.; Zhu, W.; Serda, R. E.; Franco, S.; Wang, L.; Lei, Q.; Agola, J. O.; Nouredine, A.; Ploetz, E. Modular assembly of red blood cell superstructures from metal-organic framework nanoparticle-based building blocks. *Advanced Functional Materials* **2021**, 31 (10), 2005935.

- (59) Wang, W.; Wang, L.; Huang, Y.; Xie, Z.; Jing, X. Nanoscale metal–organic framework–hemoglobin conjugates. *Chemistry–An Asian Journal* **2016**, *11* (5), 750-756.
- (60) Mandani, S.; Rezaei, B.; Ensafi, A. A.; Rezaei, P. Ultrasensitive electrochemical molecularly imprinted sensor based on AuE/Ag-MOF@ MC for determination of hemoglobin using response surface methodology. *Analytical and Bioanalytical Chemistry* **2021**, *413* (19), 4895-4906.
- (61) Martinez, D. S. T.; Paula, A. J.; Fonseca, L. C.; Luna, L. A. V.; Silveira, C. P.; Durán, N.; Alves, O. L. Monitoring the hemolytic effect of mesoporous silica nanoparticles after human blood protein corona formation. *European Journal of Inorganic Chemistry* **2015**, *2015* (27), 4595-4602.
- (62) Yu, T.; Malugin, A.; Ghandehari, H. Impact of silica nanoparticle design on cellular toxicity and hemolytic activity. *ACS nano* **2011**, *5* (7), 5717-5728.
- (63) Yildirim, A.; Ozgur, E.; Bayindir, M. Impact of mesoporous silica nanoparticle surface functionality on hemolytic activity, thrombogenicity and non-specific protein adsorption. *Journal of Materials Chemistry B* **2013**, *1* (14), 1909-1920.
- (64) Shi, J.; Hedberg, Y.; Lundin, M.; Wallinder, I. O.; Karlsson, H.; Möller, L. Hemolytic properties of synthetic nano-and porous silica particles: the effect of surface properties and the protection by the plasma corona. *Acta Biomaterialia* **2012**, *8* (9), 3478-3490.
- (65) Mukhopadhyay, S.; Veroniaina, H.; Chimombe, T.; Han, L.; Zhenghong, W.; Xiaole, Q. Synthesis and compatibility evaluation of versatile mesoporous silica nanoparticles with red blood cells: an overview. *RSC advances* **2019**, *9* (61), 35566-35578.
- (66) Tsamesidis, I.; Pouroutzidou, G. K.; Lymperaki, E.; Kazeli, K.; Lioutas, C. B.; Christodoulou, E.; Perio, P.; Reybier, K.; Pantaleo, A.; Kontonasaki, E. Effect of ion doping in silica-based nanoparticles on the hemolytic and oxidative activity in contact with human erythrocytes. *Chemico-Biological Interactions* **2020**, *318*, 108974.
- (67) Jiang, L.; Yu, Y.; Li, Y.; Yu, Y.; Duan, J.; Zou, Y.; Li, Q.; Sun, Z. Oxidative damage and energy metabolism disorder contribute to the hemolytic effect of amorphous silica nanoparticles. *Nanoscale research letters* **2016**, *11* (1), 57.
- (68) Kim, J.; Heo, Y.-J.; Shin, S. Haemocompatibility evaluation of silica nanomaterials using hemorheological measurements. *Clinical Hemorheology and Microcirculation* **2016**, *62* (2), 99-107.
- (69) Tsamesidis, I.; Kazeli, K.; Lymperaki, E.; Pouroutzidou, G. K.; Oikonomou, I. M.; Komninou, P.; Zachariadis, G.; Reybier, K.; Pantaleo, A.; Kontonasaki, E. Effect of sintering temperature of bioactive glass nanoceramics on the hemolytic activity and oxidative stress biomarkers in erythrocytes. *Cellular and Molecular Bioengineering* **2020**, *13* (3), 201-218.
- (70) Roy, P.; Saha, R.; Chakraborty, J. A novel composition of bioactive glass with potent haemostatic action and antibacterial competence. *Ceramics International* **2023**, *49* (4), 6389-6400.
- (71) Wang, Y.; Li, T.; Xie, C.; Li, S.; Lei, B. Multi-layer-structured bioactive glass nanopowder for multistage-stimulated hemostasis and wound repair. *Bioactive materials* **2023**, *25*, 319-332.
- (72) Gruian, C.; Vulpoi, A.; Vanea, E.; Oprea, B.; Steinhoff, H.-J.; Simon, S. The attachment affinity of hemoglobin toward silver-containing bioactive glass functionalized with glutaraldehyde. *The Journal of Physical Chemistry B* **2013**, *117* (51), 16558-16564.
- (73) Pourshahrestani, S.; Zeimaran, E.; Kadri, N. A.; Gargiulo, N.; Jindal, H. M.; Naveen, S. V.; Sekaran, S. D.; Kamarul, T.; Towler, M. R. Potency and cytotoxicity of a novel gallium-containing

mesoporous bioactive glass/chitosan composite scaffold as hemostatic agents. *ACS applied materials & interfaces* **2017**, 9 (37), 31381-31392.

(74) Nagrath, M.; Gallant, R.; Yazdi, A. R.; Mendonca, A.; Rahman, S.; Chiu, L.; Waldman, S. D.; Ni, H.; Towler, M. R. Tantalum-containing mesoporous bioactive glass powder for hemostasis. *Journal of Biomaterials Applications* **2021**, 35 (8), 924-932.

(75) Navati, M. S.; Friedman, J. M. Reactivity of glass-embedded met hemoglobin derivatives toward external NO: implications for nitrite-mediated production of bioactive NO. *Journal of the American Chemical Society* **2009**, 131 (34), 12273-12279.

(76) Kahbasi, S.; Samadbin, M.; Attar, F.; Heshmati, M.; Danaei, D.; Rasti, B.; Salihi, A.; Nanakali, N. M. Q.; Aziz, F. M.; Akhtari, K. The effect of aluminum oxide on red blood cell integrity and hemoglobin structure at nanoscale. *International Journal of Biological Macromolecules* **2019**, 138, 800-809.

(77) Vinardell, M.; Sordé, A.; Díaz, J.; Baccarin, T.; Mitjans, M. Comparative effects of macro-sized aluminum oxide and aluminum oxide nanoparticles on erythrocyte hemolysis: influence of cell source, temperature, and size. *Journal of nanoparticle research* **2015**, 17 (2), 80.

(78) Sabah, T.; Jawad, K. H.; Essam, N. Assessing the Toxicity of Aluminum Oxide Nanoparticles (Al₂O₃ NPS) Prepared by Laser Ablation Technique on Blood Components. *Journal of Applied Sciences and Nanotechnology* **2023**, 3 (1), 8-17.

(79) Shi, W.; Shen, Y.; Ge, D.; Xue, M.; Cao, H.; Huang, S.; Wang, J.; Zhang, G.; Zhang, F. Functionalized anodic aluminum oxide (AAO) membranes for affinity protein separation. *Journal of Membrane Science* **2008**, 325 (2), 801-808.

(80) Zaman, K.; Zaman, A.; Batcabe, J. Hematological effects of aluminum on living organisms. *Comparative Biochemistry and Physiology Part C: Pharmacology, Toxicology and Endocrinology* **1993**, 106 (2), 285-293.

(81) Wang, R.-n.; Wang, Z.-h.; Hu, W.-c.; Kong, F.-p.; Pei, Z.-y.; Song, J.; Lu, X.; Pan, B. Hemoglobin-to-red blood cell distribution width ratio in the relationship between occupational aluminum exposure and cognitive function impairment: a mediation analysis. *Frontiers in Public Health* **2025**, 13, 1639229.

(82) Abdolmajid, E.; Kharazi, H.; Chalaki, M.; Khojasteh, M.; Haghighat, S.; Attar, F.; Nemati, F.; Falahati, M. Titanium oxide nanoparticles fabrication, hemoglobin interaction, white blood cells cytotoxicity, and antibacterial studies. *Journal of Biomolecular Structure and Dynamics* **2019**, 37 (11), 3007-3017.

(83) Aliakbari, F.; Hosseinali, S. H.; Sarokhalil, Z. K.; Shahpasand, K.; Saboury, A. A.; Akhtari, K.; Falahati, M. Reactive oxygen species generated by titanium oxide nanoparticles stimulate the hemoglobin denaturation and cytotoxicity against human lymphocyte cell. *Journal of Biomolecular Structure and Dynamics* **2019**.

(84) Jia, N.; Wen, Y.; Yang, G.; Lian, Q.; Xu, C.; Shen, H. Direct electrochemistry and enzymatic activity of hemoglobin immobilized in ordered mesoporous titanium oxide matrix. *Electrochemistry communications* **2008**, 10 (5), 774-777.

(85) Amini, N.; Maleki, A. Electrochemical behavior of ticlopidine and detection of ethanol based on Hemoglobin/Ticlopidine/Titanium oxide NPs nanobiocomposite modified electrode. *Journal of Electroanalytical Chemistry* **2020**, 877, 114463.

(86) Zhou, H.; Gan, X.; Liu, T.; Yang, Q.; Li, G. Electrochemical study of photovoltaic effect of nano titanium dioxide on hemoglobin. *Bioelectrochemistry* **2006**, 69 (1), 34-40.

- (87) Sun, W.; Guo, Y.; Ju, X.; Zhang, Y.; Wang, X.; Sun, Z. Direct electrochemistry of hemoglobin on graphene and titanium dioxide nanorods composite modified electrode and its electrocatalysis. *Biosensors and Bioelectronics* **2013**, *42*, 207-213.
- (88) Huang, N.; Yang, P.; Leng, Y.; Chen, J.; Sun, H.; Wang, J.; Wang, G.; Ding, P.; Xi, T.; Leng, Y. Hemocompatibility of titanium oxide films. *Biomaterials* **2003**, *24* (13), 2177-2187.
- (89) Essandoh, M.; Garcia, R. A. Efficient removal of dyes from aqueous solutions using a novel hemoglobin/iron oxide composite. *Chemosphere* **2018**, *206*, 502-512.
- (90) Agarwal, V.; Gupta, V.; Bhardwaj, V. K.; Singh, K.; Khullar, P.; Bakshi, M. S. Hemolytic response of iron oxide magnetic nanoparticles at the interface and in bulk: extraction of blood cells by magnetic nanoparticles. *ACS Applied Materials & Interfaces* **2022**, *14* (5), 6428-6441.
- (91) Dobrovolskaia, M. A.; Clogston, J. D.; Neun, B. W.; Hall, J. B.; Patri, A. K.; McNeil, S. E. Method for analysis of nanoparticle hemolytic properties in vitro. *Nano letters* **2008**, *8* (8), 2180-2187.
- (92) Preedia Babu, E.; Subastri, A.; Suyavaran, A.; Premkumar, K.; Sujatha, V.; Aristatile, B.; Alshammari, G. M.; Dharuman, V.; Thirunavukkarasu, C. Size dependent uptake and hemolytic effect of zinc oxide nanoparticles on erythrocytes and biomedical potential of ZnO-ferulic acid conjugates. *Scientific reports* **2017**, *7* (1), 4203.
- (93) Liu, T.; Bai, R.; Zhou, H.; Wang, R.; Liu, J.; Zhao, Y.; Chen, C. The effect of size and surface ligands of iron oxide nanoparticles on blood compatibility. *RSC advances* **2020**, *10* (13), 7559-7569.
- (94) Singh, N.; Sahoo, S. K.; Kumar, R. Hemolysis tendency of anticancer nanoparticles changes with type of blood group antigen: An insight into blood nanoparticle interactions. *Materials Science and Engineering: C* **2020**, *109*, 110645.
- (95) Laranjeira, M. S.; Moco, A.; Ferreira, J.; Coimbra, S.; Costa, E.; Santos-Silva, A.; Ferreira, P. J.; Monteiro, F. J. Different hydroxyapatite magnetic nanoparticles for medical imaging: Its effects on hemostatic, hemolytic activity and cellular cytotoxicity. *Colloids and Surfaces B: Biointerfaces* **2016**, *146*, 363-374.
- (96) Muzquiz-Ramos, E.; Cortes-Hernandez, D.; Escobedo-Bocardo, J.; Zugasti-Cruz, A. In vitro bonelike apatite formation on magnetite nanoparticles after a calcium silicate treatment: Preparation, characterization and hemolysis studies. *Ceramics International* **2012**, *38* (8), 6849-6856.
- (97) Barbosa, A.; A Júnior, S.; Ferraz, A. A study of the bioactivity, hemocompatibility and antimicrobial properties of a zinc oxide and calcium phosphate composite for bone regeneration. *Cerâmica* **2023**, *69*, 93-98.
- (98) Garabagiu, S. A spectroscopic study on the interaction between gold nanoparticles and hemoglobin. *Materials Research Bulletin* **2011**, *46* (12), 2474-2477.
- (99) Shao, Q.; Wu, P.; Gu, P.; Xu, X.; Zhang, H.; Cai, C. Electrochemical and spectroscopic studies on the conformational structure of hemoglobin assembled on gold nanoparticles. *The Journal of Physical Chemistry B* **2011**, *115* (26), 8627-8637.
- (100) Drescher, D.; Büchner, T.; McNaughton, D.; Kneipp, J. SERS reveals the specific interaction of silver and gold nanoparticles with hemoglobin and red blood cell components. *Physical Chemistry Chemical Physics* **2013**, *15* (15), 5364-5373.
- (101) Egan, J. G.; Drossis, N.; Ebrilidze, I. I.; Fruehwald, H. M.; Laschuk, N. O.; Poisson, J.; de Haan, H. W.; Zenkina, O. V. Hemoglobin-driven iron-directed assembly of gold nanoparticles. *RSC advances* **2018**, *8* (28), 15675-15686.

- (102) Zhang, L.; Jiang, X.; Wang, E.; Dong, S. Attachment of gold nanoparticles to glassy carbon electrode and its application for the direct electrochemistry and electrocatalytic behavior of hemoglobin. *Biosensors and Bioelectronics* **2005**, *21* (2), 337-345.
- (103) Aseichev, A.; Azizova, O.; Beckman, E.; Skotnikova, O.; Dudnik, L.; Shcheglovitova, O.; Sergienko, V. Effects of gold nanoparticles on erythrocyte hemolysis. *Bulletin of experimental biology and medicine* **2014**, *156* (4), 495-498.
- (104) Goorani, S.; Koohi, M. K.; Morovvati, H.; Hassan, J.; Ahmeda, A.; Zangeneh, M. M. Application of natural compounds-based gold nanoparticles for the treatment of hemolytic anemia in an anemic mouse model: Formulation of a novel drug from relationship between the nanotechnology and hematology sciences. *Applied organometallic chemistry* **2020**, *34* (4), e5475.
- (105) Purohit, R.; Vallabani, N. S.; Shukla, R. K.; Kumar, A.; Singh, S. Effect of gold nanoparticle size and surface coating on human red blood cells. *Bioinspired, Biomimetic and Nanobiomaterials* **2016**, *5* (3), 121-131.
- (106) Devi, L. B.; Das, S. K.; Mandal, A. B. Impact of surface functionalization of AgNPs on binding and conformational change of hemoglobin (Hb) and hemolytic behavior. *The Journal of Physical Chemistry C* **2014**, *118* (51), 29739-29749.
- (107) Choi, J.; Reipa, V.; Hitchins, V. M.; Goering, P. L.; Malinauskas, R. A. Physicochemical characterization and in V itro hemolysis evaluation of silver nanoparticles. *Toxicological Sciences* **2011**, *123* (1), 133-143.
- (108) Chen, L. Q.; Fang, L.; Ling, J.; Ding, C. Z.; Kang, B.; Huang, C. Z. Nanotoxicity of silver nanoparticles to red blood cells: size dependent adsorption, uptake, and hemolytic activity. *Chemical research in toxicology* **2015**, *28* (3), 501-509.
- (109) Bhunia, A. K.; Samanta, P. K.; Aich, D.; Saha, S.; Kamilya, T. Biocompatibility study of protein capped and uncapped silver nanoparticles on human hemoglobin. *Journal of Physics D: Applied Physics* **2015**, *48* (23), 235305.
- (110) Chi, Z.; Lin, H.; Li, W.; Zhang, X.; Zhang, Q. In vitro assessment of the toxicity of small silver nanoparticles and silver ions to the red blood cells. *Environmental Science and Pollution Research* **2018**, *25* (32), 32373-32380.
- (111) Zolghadri, S.; Saboury, A.; Golestani, A.; Divsalar, A.; Rezaei-Zarchi, S.; Moosavi-Movahedi, A. Interaction between silver nanoparticle and bovine hemoglobin at different temperatures. *Journal of Nanoparticle Research* **2009**, *11* (7), 1751-1758.
- (112) Bhunia, A. K.; Kamilya, T.; Saha, S. Study of the adsorption of human hemoglobin to silver (Ag) nanoparticle surface for the detection of the unfolding of hemoglobin. *Plasmonics* **2022**, *17* (3), 1139-1156.
- (113) Bhunia, A.; Kamilya, T.; Saha, S. Silver nanoparticle-human hemoglobin interface: time evolution of the corona formation and interaction phenomenon. *Nano Convergence* **2017**, *4* (1), 28.
- (114) Beg, M.; Maji, A.; Mandal, A. K.; Das, S.; Jha, P. K.; Hossain, M. Spectroscopic investigation on interaction of biogenic, Croton bonplandianum leaves extract mediated potential bactericidal silver nanoparticles with human hemoglobin and human serum albumin. *Journal of Biomolecular Structure and Dynamics* **2018**, *36* (3), 711-723.
- (115) Das, P.; Saha, S.; Guha, P. K.; Bhunia, A. K. Quantum dot-protein interface: Interaction of the CdS quantum dot with human hemoglobin for the study of the energy transfer process and

binding mechanism along with detection of the unfolding of hemoglobin. *Spectrochimica Acta Part A: Molecular and Biomolecular Spectroscopy* **2025**, 324, 124937.

(116) Shen, X.-C.; Liou, X.-Y.; Ye, L.-P.; Liang, H.; Wang, Z.-Y. Spectroscopic studies on the interaction between human hemoglobin and CdS quantum dots. *Journal of colloid and interface science* **2007**, 311 (2), 400-406.

(117) Wang, Q.; Chen, W.-Q.; Liu, X.-Y.; Liu, Y.; Jiang, F.-L. Thermodynamic implications and time evolution of the interactions of near-infrared PbS quantum dots with human serum albumin. *ACS omega* **2021**, 6 (8), 5569-5581.

(118) Ba, X.-X.; Gao, T.; Yang, M.; Jiang, P.; Jiang, F.-L.; Liu, Y. Thermodynamics of the interaction between graphene quantum dots with human serum albumin and γ -globulins. *Journal of Solution Chemistry* **2020**, 49 (1), 100-116.

(119) Wang, Y.; Han, Q.; Zhang, H.; Shi, J.; Shen, Y.; Zhang, Y.; Wang, Y. Binding interactions of MoS₂ quantum dots with hemoglobin and their adsorption isotherms and kinetics in vitro. *Journal of Molecular Liquids* **2019**, 275, 304-311.

(120) Farsaci, F.; Tellone, E.; Galtieri, A.; Ficarra, S. A new model for thermodynamic characterization of hemoglobin. *Fluids* **2019**, 4 (3), 135.

(121) Patil, S.; Pancholi, S.; Agrawal, S.; Agrawal, G. Surface-modified mesoporous ceramics as delivery vehicle for haemoglobin. *Drug delivery* **2004**, 11 (3), 193-199.

(122) Li, S.; Du, K. Self-sacrificing template synthesis of ultralight porous hydroxyapatite microtube-based ceramics for hemoglobin adsorption. *Chemical Engineering Journal* **2024**, 492, 152404.

(123) Aich, A.; Pan, W.; Vekilov, P. G. Thermodynamic mechanism of free heme action on sickle cell hemoglobin polymerization. *AIChE Journal* **2015**, 61 (9), 2861-2870.

(124) Vekilov, P. G.; Galkin, O.; Pettitt, B. M.; Choudhury, N.; Nagel, R. L. Determination of the transition-state entropy for aggregation suggests how the growth of sickle cell hemoglobin polymers can be slowed. *Journal of molecular biology* **2008**, 377 (3), 882-888.

(125) Minton, A. P. A thermodynamic model for gelation of sickle-cell hemoglobin. *Journal of Molecular Biology* **1974**, 82 (4), 483-498.

(126) Uzunova, V. V.; Pan, W.; Galkin, O.; Vekilov, P. G. Free heme and the polymerization of sickle cell hemoglobin. *Biophysical journal* **2010**, 99 (6), 1976-1985.

(127) Magdoff-Fairchild, B.; Poillon, W. N.; Li, T.-I.; Bertles, J. F. Thermodynamic studies of polymerization of deoxygenated sickle cell hemoglobin. *Proceedings of the National Academy of Sciences* **1976**, 73 (4), 990-994.

(128) Vekilov, P. G.; Feeling-Taylor, A. R.; Petsev, D. N.; Galkin, O.; Nagel, R. L.; Hirsch, R. E. Intermolecular interactions, nucleation, and thermodynamics of crystallization of hemoglobin C. *Biophysical journal* **2002**, 83 (2), 1147-1156.

(129) Sovadinova, I.; Palermo, E. F.; Huang, R.; Thoma, L. M.; Kuroda, K. Mechanism of polymer-induced hemolysis: nanosized pore formation and osmotic lysis. *Biomacromolecules* **2011**, 12 (1), 260-268.

(130) Gilson, M. K.; Given, J. A.; Bush, B. L.; McCammon, J. A. The statistical-thermodynamic basis for computation of binding affinities: a critical review. *Biophysical journal* **1997**, 72 (3), 1047-1069.

(131) Jarillo, J.; Morín, J. A.; Beltrán-Heredia, E.; Villaluenga, J. P.; Ibarra, B.; Cao, F. J. Mechanics, thermodynamics, and kinetics of ligand binding to biopolymers. *PLoS One* **2017**, 12 (4), e0174830.

- (132) Johnson, E. R.; Becke, A. D. A post-Hartree-Fock model of intermolecular interactions: Inclusion of higher-order corrections. *The Journal of chemical physics* **2006**, *124* (17).
- (133) Moy, G.; Corry, B.; Kuyucak, S.; Chung, S.-H. Tests of continuum theories as models of ion channels. I. Poisson– Boltzmann theory versus Brownian dynamics. *Biophysical Journal* **2000**, *78* (5), 2349-2363.
- (134) van Oss, C. J. The extended DLVO theory. In *Interface Science and Technology*, Vol. 16; Elsevier, 2008; pp 31-48.
- (135) Liu, Y.-M.; Zheng, Y.-Y.; Lin, H.-J.; Wei, P.-C.; Fan, Q.-C.; Huang, G.-G.; Meng, D. Calculation of contact angle via Young-Dupré equation with molecular dynamic simulation: Kaolinite as an example. *Colloids and Surfaces A: Physicochemical and Engineering Aspects* **2024**, *697*, 134469.
- (136) Schmidt, M.; Brader, J. M. Power functional theory for Brownian dynamics. *The Journal of chemical physics* **2013**, *138* (21).
- (137) Zhou, H. X.; Szabo, A. Microscopic formulation of Marcus' theory of electron transfer. *The Journal of chemical physics* **1995**, *103* (9), 3481-3494.
- (138) Lin, Y.; Pan, D.; Li, J.; Zhang, L.; Shao, X. Application of Berendsen barostat in dissipative particle dynamics for nonequilibrium dynamic simulation. *The Journal of Chemical Physics* **2017**, *146* (12).
- (139) Fukuda, I.; Moritsugu, K. Coupled Nosé-Hoover equations of motion to implement a fluctuating heat-bath temperature. *Physical Review E* **2016**, *93* (3), 033306.
- (140) Martoňák, R.; Laio, A.; Parrinello, M. Predicting crystal structures: the Parrinello-Rahman method revisited. *Physical review letters* **2003**, *90* (7), 075503.
- (141) Reed, M. B. L-Broyden methods: a generalization of the L-BFGS method to the limited-memory Broyden family. *International Journal of Computer Mathematics* **2009**, *86* (4), 606-615.